

A numerical model simulating reactive transport and evolution of fracture permeability

Hideaki Yasuhara^{1,*†} and Derek Elsworth²

¹*Department of Civil and Environmental Engineering, Ehime University, 3 Bunkyo-cho, Matsuyama 790-8577, Japan*

²*Department of Energy and Geo-Environmental Engineering, Penn State University, University Park, PA 16802, U.S.A.*

SUMMARY

A numerical model is presented to describe the evolution of fracture aperture (and related permeability) mediated by the competing chemical processes of pressure solution and free-face dissolution/precipitation; pressure (dis)solution and precipitation effect net-reduction in aperture and free-face dissolution effects net-increase. These processes are incorporated to examine coupled thermo-hydro-mechano-chemo responses during a flow-through experiment, and applied to reckon the effect of forced fluid injection within rock fractures at geothermal and petroleum sites. The model accommodates advection-dominant transport systems by employing the Lagrangian–Eulerian method. This enables changes in aperture and solute concentration within a fracture to be followed with time for arbitrary driving effective stresses, fluid and rock temperatures, and fluid flow rates. This allows a systematic evaluation of evolving linked mechanical and chemical processes. Changes in fracture aperture and solute concentration tracked within a well-constrained flow-through test completed on a natural fracture in novaculite (*Earth Planet. Sci. Lett.* 2006, in press) are compared with the distributed parameter model. These results show relatively good agreement, excepting an enigmatic abrupt reduction in fracture aperture in the early experimental period, suggesting that other mechanisms such as mechanical creep and clogging induced by unanticipated local precipitation need to be quantified and incorporated. The model is applied to examine the evolution in fracture permeability for different inlet conditions, including localized (rather than distributed) injection. Predictions show the evolution of preferential flow paths driven by dissolution, and also define the sense of permeability evolution at field scale. Copyright © 2006 John Wiley & Sons, Ltd.

KEY WORDS: fracture permeability; Lagrangian–Eulerian method; dissolution

1. INTRODUCTION

Coupled thermal–hydraulic–mechanical–chemical (THMC) processes exert significant influence in controlling the evolution of the mechanical and transport properties for fractured rocks. The

*Correspondence to: Hideaki Yasuhara, Department of Civil and Environmental Engineering, Ehime University, 3 Bunkyo-cho, Matsuyama 790-8577, Japan.

†E-mail: hide@dpc.ehime-u.ac.jp

Contract/grant numbers: DOE-DE-PS26-01NT41048, DOE-DE-FG36-04GO14289, ARC DP0209425

Received 31 August 2005

Revised 23 January 2006

Accepted 23 February 2006

competition between agents that reduce porosity (grain interpenetration, compaction, pressure solution, and precipitation) and those that generate porosity (dilation and free-face dissolution) control the rates, magnitudes, and sense of permeability modification, strength gain, and change in stiffness. In turn, these processes are important in defining the evolution of porosity and permeability in subsiding basins, in geothermal and petroleum reservoirs, and around repositories for the entombment of radioactive wastes, and in defining rates and magnitudes of strength gain that impact recurrence times and magnitudes of earthquakes.

To better understand the effects of temperature, stress, and fluid chemistry on the evolution of fracture permeability, only a limited number of experiments have been conducted under hydrothermal conditions, indicating the conflicting predictions on evolution in fracture permeability; sealing, gapping, or spontaneous switching between sealing and gapping is observed to result from net dissolution or precipitation within a fracture. Dissolution-driven sealing, likely resulting from dissolution beneath propping asperities in contact, is reported for natural and artificial fractures at elevated temperatures ($> 300^{\circ}\text{C}$) in sandstone [1, 2], in granite [3], and in quartz [4], and at modest temperatures ($50\text{--}150^{\circ}\text{C}$) in tuff [5] and in novaculite [6]. These are supplemented by results at both high confining stress ($> 150\text{ MPa}$) in granite [7] and at low stress (0.2 MPa) in marble where an acidic permeant is circulated [8]. Conversely, precipitation-driven sealing is observed in tuff at a range of temperatures [9]. Gapping is observed in hydrocarbon reservoir rocks [10, 11], and spontaneous or induced switching from sealing to gapping is reported at ambient temperatures (20°C) in limestone [12] and at modest temperatures ($20\text{--}120^{\circ}\text{C}$) in novaculite [13]. These limited studies on fractures provide no conclusive view of the effects controlling the evolution of the transport properties, and the evolving rates and magnitudes of fracture permeability driven by interaction between the mechanical and chemical processes remain poorly constrained.

Modelling studies are an important supplement to experimental observations of the evolution in the transport properties of fractures under hydrothermal conditions. Such studies allow complexly interacting processes to be unraveled, to explain counter-intuitive results. These models must incorporate the interactions of reactive mass transport and mechanical effects, with these approaches complicated where flows are advection dominant—as they may be for flows in fractures. Difficulties result in accurately solving using numerical methods where flows are dominated by advective transport since numerical oscillation may result for Eulerian approaches where local Peclet numbers are large. To circumvent this problem, a variety of numerical treatments may be employed; the easiest involving a reduction in the spatial element (or grid) size. However, for very large velocities, this treatment is not always practical, due to the requisite large number of elements. For purely advective flows, Eulerian methods are intrinsically unstable, and erroneous oscillations may not be removed. Upstream-weighted finite element (FEM) and finite difference (FDM) methods may enable oscillations to be eliminated for high Peclet numbers, but these methods may generate artificial or numerical dispersion, resulting from their incapacity to preserve the sharpness of the front (or steep concentration gradients). An alternative to these flawed methods is the mixed Lagrangian–Eulerian approach [14–16] that overcomes many of the innate problems in high velocity flows. This method accommodates the advection term through a Lagrangian approach—the advective component is solved by tracking particles along characteristic pathlines, with all other terms in the solute-transport equation solved from an Eulerian viewpoint on a grid fixed in space. This method has the advantage that numerical oscillations and artificial dispersion are automatically

damped, and the procedure may continuously handle problems with mesh Courant numbers in excess of unity.

In this study, a Lagrangian–Eulerian algorithm is presented to follow the progress of evolution in permeability when a fracture is subjected to chemical dissolution by circulating hydrothermal fluids. Notably, our focuses are in examining the chemical processes that significantly influence the evolution in fracture permeability and in accommodating evolving advection-dominant transport problems. To demonstrate capability and validity of the model, predictions are compared with a companion flow-through experiment conducted on a stressed natural fracture in novaculite (> 99.5% quartz) [13].

2. MODEL DESCRIPTION

A numerical model is developed to describe the stress- and temperature-dependent evolution in aperture (permeability) within a single fracture mediated by chemical dissolution. This model accommodates solution for fluid flow and solute transport processes under advection-dominant conditions. The virtual fracture is constructed using the exact topography of two rough surfaces in contact, which have been previously profiled in 3-D [17]. From this prescribed initial aperture distribution within the fracture, and assuming steady conditions, the fluid velocity field is calculated from the Reynolds approximation. The local rate of dissolution/precipitation throughout the whole fracture domain is then determined, and the updated concentration distribution is obtained. Subsequently, the new aperture distribution resulting from chemical reaction is updated, and the final concentration distribution is obtained by solving the advection–diffusion equation. Each calculation process is explained in detail in the following.

2.1. FE mesh

The rectilinear two-dimensional mesh occupies the mean plane of the fracture and uses data from the measured topography of two rough surfaces in contact—the profile measured by 3-D roughness profiling (for details, see References [13, 17]). Each node in the fracture mesh has a local aperture datum that may be determined simply by point-by-point subtraction of the two digitized surfaces. However, careful positioning and orientation of the two surfaces is required before the subtraction since the profiles are initially unmated—the upper and lower rough surfaces are measured in an open-book format. To limit skewing of the aperture data, the mean planes of both surfaces are calculated and are made parallel to each other [18].

Figure 1 shows the parallel digitized rough surfaces of a natural fracture in novaculite. The differenced surface (i.e. the point-by-point subtraction of two surfaces) represents the distribution of the mechanical aperture, rather than the hydraulic aperture recovered from the flow-through experimental results. However, as a first-order estimation, the arithmetic mean aperture of the initial differenced surface is used for model prediction. This is calibrated by adjusting the separation between the two virtual parallel surfaces, and setting the initial hydraulic aperture to that obtained from the experiment [13]—mechanical and hydraulic apertures are assumed approximately equivalent [18].

Note that at contact points between the rough surfaces, a finite thickness water-film is assumed. This allows diffusive transport of mineral mass dissolved and then mobilized at these contacts by the elevated chemical potential beneath the stressed surface. Such a thin water-film

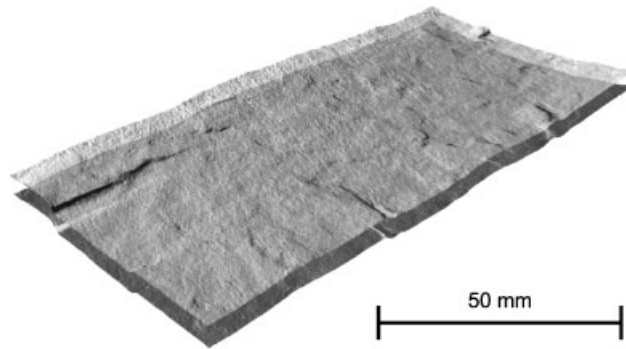


Figure 1. Oblique view of the parallel rough surfaces digitized by the 3-D laser profilometer system. The digitized surface measures $50 \times 89.5 \text{ mm}^2$.

at the contact may be a function of applied stress and may range from less than 1 nm to a few hundreds nanometers [19, 20]. In this study, we presume a constant water-film thickness, ω , of 4.0 nm as this thickness remains ill-constrained.

2.2. Fluid flow distribution

The FE mesh of the fracture aperture distribution is utilized for fluid flow simulations. The flow simulation is conducted using the steady-state approximation of the Navier–Stokes equation for incompressible laminar flow (the Reynolds approximation) [21, 22] as

$$\nabla \cdot \left(\frac{b^3}{12\mu} \nabla p \right) = 0 \quad (1)$$

where b is the local aperture, μ is the fluid viscosity, and p is the fluid pressure driving flow. This returns a steady distribution of velocity, which is updated as the aperture distribution changes. Although the Reynolds equation is known to overestimate fluid velocity when fracture aperture is small relative to surface roughness [23], this error is small in relation to the other uncertainties within the analysis.

2.3. Pressure solution and free-face dissolution

Dissolution-dependent evolution of the fracture aperture is controlled by the competing influences of pressure (dis)solution and free-face dissolution. Fracture aperture (or related permeability) may decrease if pressure solution dominates, or may increase if free-face dissolution prevails. Pressure solution within a fracture incorporates three serial processes; dissolution at asperity contacts, diffusion along the interfacial water-film, and precipitation at the pore (fracture) wall, and may result in net reduction of fracture aperture. Conversely, if the mass rate of supply to the fluid occupying the fracture void is sufficiently low, or the flow-system sufficiently open, then the solute concentration in the pore fluid will be below the equilibrium concentration, net dissolution at free walls may dominate, and the fracture will widen. The competition between pressure solution and precipitation in the fracture void, that together contribute to a net reduction in permeability, and dissolution from the wall of the fracture void, that increases permeability, will prescribe the dominant effect; either net sealing or gapping.

Importantly, the dominant mechanism may change with stress and chemical condition of the solvent, or as a result of the evolution of fracture topography, and flow topology.

Here, stress- and temperature-dependent dissolution at contacting asperities and free-face dissolution/precipitation are systematically defined. First, dissolution at the asperity contacts provides a source of mass into the fracture cavity. Applying nonhydrostatic and nonequilibrium thermodynamics and then considering the chemical potential difference between the compressive site of contact and the less-stressed site of the pore wall, that is the motive force driving pressure solution, the source of mass injected into the fracture void space is most conveniently defined in terms of a dissolution mass flux, $dM_{\text{diss}}^{\text{PS}}/dt$, given as (for details, see Reference [24]),

$$\frac{dM_{\text{diss}}^{\text{PS}}}{dt} = \frac{3V_m^2(\sigma_a - \sigma_c)k_+\rho_g A_c}{RT} \quad (2)$$

where V_m is molar volume of the solid ($2.27 \times 10^{-5} \text{ m}^3 \text{ mol}^{-1}$ for quartz), σ_a is the disjoining pressure [25] equal to the amount by which the pressure acting at a contact area exceeds the hydrostatic pore pressure, k_+ is the dissolution rate constant of the solid, ρ_g is the solid density (2650 kg m^{-3} for quartz), A_c is the size of the local contact area, R is the gas constant, and T is the temperature of the system. σ_c is the critical stress that defines stress state where the compaction of indenting asperity contacts will effectively halt. Where confining stress is applied to a rock fracture, asperity indentation will occur as a result of high localized contact stresses. Transient interpenetration may develop by plastic creep as the contact stress remains in excess of a critical stress, σ_c . Where stresses remain in excess of the critical interpenetration stress, dissolution will proceed in the water-film enveloping the interface, and mass will be removed by dissolution and transported by diffusion. This process will continue until the applied contact stress is sufficiently reduced by the growth of the contact area that compaction essentially ceases. The limiting stress may be defined by considering the energy balance under applied stress and temperature conditions, given by Revil [26] modified from Reference [27],

$$\sigma_c = \frac{E_m(1 - T/T_m)}{4V_m} \quad (3)$$

where E_m and T_m are the heat and temperature of fusion, respectively ($E_m = 8.57 \text{ kJ mol}^{-1}$, $T_m = 1883 \text{ K}$ for quartz).

Next, free-face dissolution and precipitation components are quantified as mass fluxes, $dM_{\text{diss}}^{\text{FF}}/dt$ and dM_{prec}/dt , defined by the dissolution/precipitation rate constants and the difference between the fluid mass concentration in the pore space and the equilibrium concentration, defined as (modified from Reference [28]),

$$\frac{dM_{\text{diss}}^{\text{FF}}}{dt} = k_+ A_{\text{pore}} \rho_g V_m \left(1 - \left(\frac{C_{\text{pore}}}{C_{\text{eq}}} \right)^m \right)^n \quad (4)$$

$$\frac{dM_{\text{prec}}}{dt} = k_- A_{\text{pore}} \rho_g V_m \left(\left(\frac{C_{\text{pore}}}{C_{\text{eq}}} \right)^m - 1 \right)^n \quad (5)$$

where A_{pore} is the area of the fracture void, k_- is the precipitation rate constant of the dissolved mineral, C_{pore} is the concentration in the pore space, and C_{eq} is the equilibrium solubility of the dissolved mineral. m and n are two positive numbers normally constrained by experiment; for quartz–water reaction, the reaction kinetics is likely first order [29], and in the model m and n are set to unity. Note that the free-face dissolution/precipitation mass fluxes will be zero as the mass

concentration in the pore fluid is either greater or smaller than the equilibrium solubility, respectively.

Dissolution/precipitation rate constant $k_{+/-}$, equilibrium solubility C_{eq} , and diffusion coefficient D of quartz have all Arrhenius-type dependence with temperature, given by

$$k_+ = k_+^0 \exp(-E_{k_+}/RT) \quad (6)$$

$$k_- = k_-^0 \exp(-E_{k_-}/RT) \quad (7)$$

$$C_{\text{eq}} = C_{\text{eq}}^0 \exp(-E_C/RT) \quad (8)$$

$$D = D_0 \exp(-E_D/RT) \quad (9)$$

Appropriate magnitudes are selected for these constants defining the temperature dependence as, $k_{+/-}^0 = 1.59/1.27 \text{ mol m}^2 \text{ s}^{-1}$ and $E_{k_{+/-}} = 71.3/48.9 \text{ kJ mol}^{-1}$ [30], $C_{\text{eq}}^0 = 274.9 \text{ kg m}^{-3}$ and $E_C = 26.4 \text{ kJ mol}^{-1}$ [31], and $D_0 = 5.2 \times 10^{-8} \text{ m}^2 \text{ s}^{-1}$ and $E_D = 13.5 \text{ kJ mol}^{-1}$ [26].

2.4. Lagrangian–Eulerian approach

The solute transport in a fracture is modelled by the mixed Lagrangian–Eulerian approach. An advection–diffusion equation is given as

$$\frac{\partial M}{\partial t} + \mathbf{V} \cdot \nabla M = D \nabla^2 M \quad (10)$$

where M denotes the mass of the solute, \mathbf{V} is the velocity, and D is the diffusion coefficient. The diffusion coefficient of the solute may be different between contact and void nodes. The diffusivity inside contacts may be a few orders of magnitudes smaller than that in the bulk pore fluid due to electro-viscous effects [32, 33], although others [34] justify that this has minor influence. Correspondingly, we use the same value of the diffusion coefficient for both contact and void points.

Applying the Galerkin FEM Equation (10) may be written in discrete form for the Lagrangian–Eulerian approach, as [15]

$$\left[\int_R N_i N_i \, dR \right] \frac{DM_i}{Dt} + \left[\int_R (\nabla N_i) D (\nabla N_i) \, dR \right] M_i = \int_B D \cdot (\nabla M) \cdot n N_i \, dB \quad (i = 1, 2, \dots, N) \quad (11)$$

where

$$\frac{D}{Dt} = \frac{\partial}{\partial t} + \mathbf{V} \cdot \nabla \quad (12)$$

in which N_i is the shape function at the i th node, DM_i/Dt is the Lagrangian derivative of M_i with respect to time, R is the region of interest, B is the global boundary, and N is the total number of the nodes in the system. Integrating Equation (11) using explicit time stepping, linear interpolation, and a fixed time step Δt , yields,

$$([W]/\Delta t + [K])\{M^{n+1}\} = ([W]/\Delta t)\{M^*\} + \{B\} \quad (13)$$

where

$$[W] = \sum \left(\int_R N_i N_i \, dR \right) \quad (14)$$

$$[K] = \sum \left(\int_R (\nabla N_i) D (\nabla N_i) dR \right) \tag{15}$$

$$\{B\} = \sum \left(\int_B D \cdot (\nabla M) \cdot n N_i dB \right) \tag{16}$$

in which $\{M^{n+1}\}$ is the mass at the new time and $\{M^*\}$ is the Lagrangian mass. To obtain the Lagrangian mass at t^{n+1} , a forward-particle-tracked mass M_j^p , is first computed during time step Δt , given as

$$M_j^p = M(\mathbf{x}_j^*, t^{n+1}) = M_j^n \quad (j = 1, 2, \dots, N) \tag{17}$$

where

$$\mathbf{x}_j^* = \mathbf{x}_j^n + \mathbf{V}_j \Delta t \quad (j = 1, 2, \dots, N) \tag{18}$$

in which \mathbf{x}_j^* is the fictitious particle position at t^{n+1} when travelling from nodal location \mathbf{x}_j^n at t^n . Subsequently, applying FE interpolation with the shape functions, the Lagrangian mass M_i^* at each node is evaluated as (see Figure 2),

$$M_i^* = \sum_{j=1}^N M_j^p N_j(\mathbf{x}_i) \quad (i = 1, 2, \dots, N) \tag{19}$$

Once the Lagrangian mass M_i^* is obtained, the final mass M_i^{n+1} at t^{n+1} is computed using Equation (13).

Careful treatment is required for no-flow boundaries. Solutes are not allowed to cross no-flow boundaries, but for certain choices of large time steps, particles may be inadvertently ejected, as illustrated in Figure 3. This condition may be corrected by relocating the escaping particle back into the flow-field by using its closest projection to the boundary, as illustrated in Figure 3. This correction will thus tend to return the particle close to its true flow trajectory.

2.5. Overall computational procedure

With the fracture topography digitized, the flow simulation defines the initial flow velocity field. Mineral mass is either injected-into, or removed-from, the flow-field, depending on the relative dominance of processes of pressure solution and free-face dissolution/precipitation. These components are then transported within the fluid phase, until conditions dictate their removal to

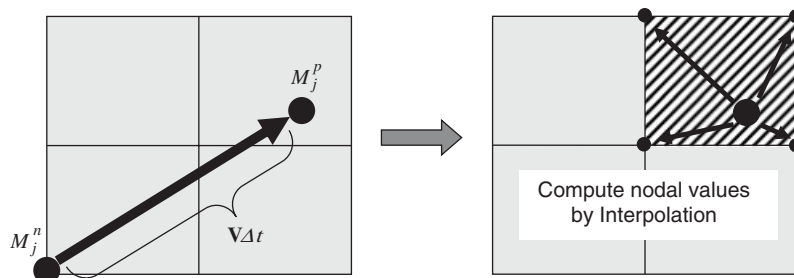


Figure 2. Schematic illustration of computing the Lagrangian mass at the nodal locations. During time step Δt , the nodal mass M_j^n travels to M_j^p , and the new nodal values are interpolated using shape functions.

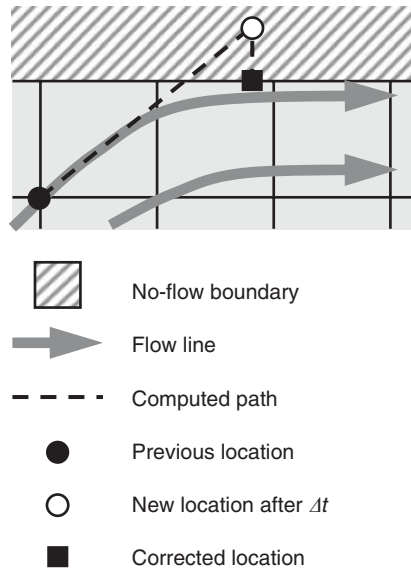


Figure 3. Schematic of correction applied to the computed particle location near no-flow boundary.

the fracture walls. Importantly, prior characterizations of an interface region as a separate diffusive domain [35], are unnecessary, as mass diffusion within the water-film separating contacts is automatically accommodated by the macro-scale FE mesh. Note that the flow simulation, the chemical processes, and the solute transport equation are solved sequentially, rather than simultaneously. The main points of the computational procedure are as follows.

First, the initial fracture topography is set to generate the FE mesh—each node has a local aperture datum. Second, the initial and boundary conditions (i.e. temperatures, stresses, flow rates, and flow or no-flow boundaries) are applied, and flow simulation (Equation (1)) is conducted using the aperture mesh to obtain the distribution of flow velocities within the fracture. The simulation retrieves elemental velocities at Gauss points, and nodal velocities are interpolated using shape functions to accommodate solving the solute transport equation (i.e. obtaining the fictitious particle position using nodal velocity as shown in Equation (18)).

Third, the dissolution/precipitation processes at contact points and void wall are evaluated using Equations (2)–(5) at every single node. In Equation (2), the stress acting at contact points σ_a is simply defined by,

$$\sigma_a = \sigma_{\text{eff}} \frac{n_c}{n_t} \quad (20)$$

where σ_{eff} is the confining effective stress prescribed. n_c and n_t is the numbers of contact points and total nodes, respectively. This assumes that the contacting stresses are equivalent at all contact areas distributed within the fracture. The effective area for pressure dissolution (i.e. A_c) is assumed equal to the area of a single element, and that for free-face dissolution/precipitation (i.e. A_{pore}) is assumed equal to twice the elemental area (both upper and lower void walls

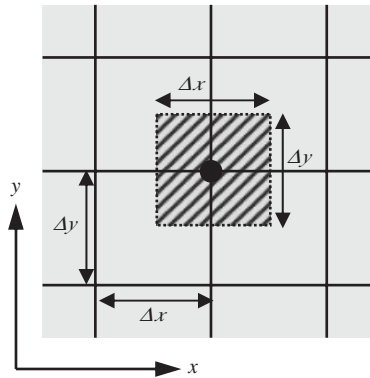


Figure 4. Representation of contact or void area (shaded area) at each node for chemical calculations. The effective area for pressure dissolution and free-face dissolution/precipitation is equivalent to either the area of a single element, or twice that area, respectively.

contribute) (Figure 4). Consequently, the nodal aperture b_i at t^{n+1} is calculated as

$$b_i^{n+1} = b_i^n - \frac{dM_{\text{diss}}^{\text{PS}}}{dt} \frac{\Delta t}{\rho_g A_e} + \left(\frac{dM_{\text{diss}}^{\text{FF}}}{dt} \Big|_i - \frac{dM_{\text{prec}}}{dt} \Big|_i \right) \frac{\Delta t}{\rho_g A_e} \quad (i = 1, 2, \dots, N) \quad (21)$$

where A_e is the area of an element. If b_i^{n+1} becomes smaller than the water-film thickness of 4 nm, it is then indexed as a contacting node and $b_i^{n+1} = 4.0$ nm. Simultaneously, the nodal mass dissolved is also updated as

$$M_i^{c,n+1} = M_i^n - \frac{dM_{\text{diss}}^{\text{PS}}}{dt} \Delta t \quad (\text{if } b_i^{n+1} = 4.0 \text{ nm}) \quad (22)$$

$$M_i^{c,n+1} = M_i^n - \left(\frac{dM_{\text{diss}}^{\text{FF}}}{dt} \Big|_i - \frac{dM_{\text{prec}}}{dt} \Big|_i \right) \Delta t \quad (\text{if } b_i^{n+1} > 4.0 \text{ nm}) \quad (23)$$

where $M_i^{c,n+1}$ ($i = 1, 2, \dots, N$) is the updated mass at each node after the incremented time, but is not the final one at t^{n+1} since it is subsequently modified by solute transport.

Finally, the contribution of solute transport (Equation (10)) is computed using the Lagrangian–Eulerian approach. The final mass at t^{n+1} is calculated as schematically shown in Figure 5. Then, the concentration at each node is evaluated using the updated mass at t^{n+1} , given as

$$C_i^{n+1} = \frac{M_i^{n+1}}{b_i^{n+1} A_e} \quad (i = 1, 2, \dots, N) \quad (24)$$

The updated concentrations are used to calculate free-face dissolution/precipitation (Equations (4) and (5)) at the next time step. The lumped concentration travelling out of the domain C_{out}^{n+1} , which is directly analogous to mineral efflux measurements made during the experiments, is also calculated by

$$C_{\text{out}}^{n+1} = \frac{\sum M_{\text{out}}^{n+1}}{Q \Delta t} \quad (25)$$

where $\sum M_{\text{out}}^{n+1}$ is the summation of the solute mass exiting the outflow boundary during one time increment, and Q is the flow rate.

In summary, the combined algorithm incorporates an initial evaluation of aperture distribution from profile data, fluid transport simulation, and subsequent evaluation of mineral mass transport and redistribution, as outlined in Figure 6. This procedure allows the evolution

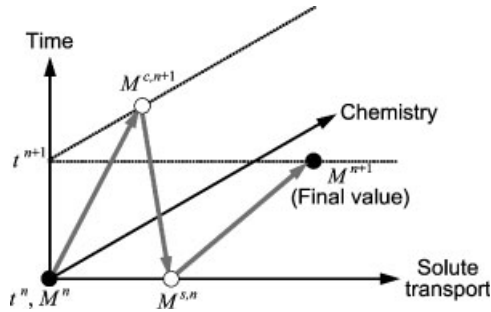


Figure 5. Schematic of calculation sequence during incremental time to obtain nodal mass, involving chemical processes and solute transport. Note that $M^{c,n+1} = M^{s,n}$.

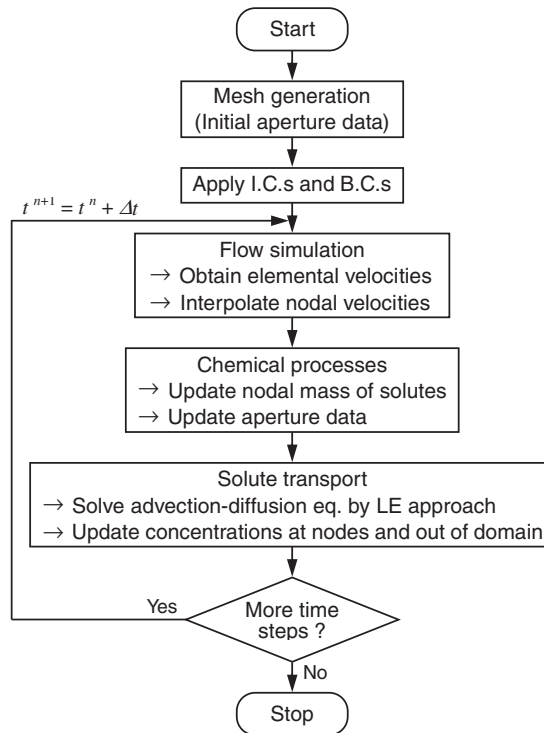


Figure 6. Flow chart for the overall computational procedure.

of fracture aperture to be followed where stress, temperature, and fluid flow conditions mediate behaviour.

3. COMPARISON WITH EXPERIMENTAL MEASUREMENTS

This numerical model is applied to describe the time-dependent evolution in aperture obtained from a companion experiment in a stressed natural fracture of novaculite [13]. The flow-through experiment is conducted on a natural fracture of Arkansas novaculite, which has a uniform grain size in the range 1–6 μm and high quartz content of > 99.5% [36], at a constant effective stress of 1.38 MPa (200 psi) and at elevated temperatures in the range 20–120°C. Distilled water is used as a permeant and thus, the chemical system is relatively simple (i.e. $\text{SiO}_2 + 2\text{H}_2\text{O} \leftrightarrow \text{Si}(\text{OH})_4$). The experimental conditions during the entire length of experiments (3150 h) are listed in Table I.

Prior to applying the current model, the lumped parameter model previously developed [35,37] is first adopted to predict the progress of mean aperture closure and evolution of Si efflux, for the same experiment. Then, the current model is applied to quantify the experimental observations, and predictions given by the two different models are compared and examined, relative to the experimental measurements.

3.1. Lumped parameter model comparison

Lumped parameter models [35,37] are capable of approximately representing the principal chemical processes of pressure solution at mineral contacts, solute diffusion along these contacts, and precipitation on the void wall of a fracture at a single representative contact. These solutions may also represent free-face dissolution, together with changes in fracture aperture and mineral mass concentration in the effluent fluid that result. These solutions are approximate in that they require a single representative contact to be defined—all processes at the contacting walls, and in the void, are averages of the entire contact area and void volume, respectively. Importantly, characteristic differences of the lumped parameter model from the numerical model developed in Section 2 are that fracture topography is simplified by a representative contact surrounded by an appropriate tributary area (see Figure 7) and that a

Table I. Experimental conditions [37].

Time (h)	Temperature (°C)	Flow rate (mL min^{-1})	Flow direction
0–121	20	1.0	Original
121–380	20	0.5	Original
380–858	20	0.25	Original
858–930	20	0.0	—
930–1266	20	0.25	Original
1266–1292	20	0.125	Original
1292–1494	20	0.125	Reversed
1494–1869	20	0.0625	Original
1869–2255	40	0.0625	Original
2255–2875	80	0.0625	Original
2875–3150	120	0.125	Original

simple, but physically plausible, relation between fracture aperture and fracture contact-area ratio is defined to represent the irreversible alteration in fracture geometry caused by pressure solution and free-face dissolution. Correspondingly, processes are innately averaged, and no account is made for the spatial structure. Such models typically make adequate predictions of homogeneously distributed behaviours, but not of localized effects, such as the evolution of a through-going dissolution conduit (wormhole) [12, 37].

The digitized fracture obtained through the profiling data constrains the relation between the fracture aperture and the contact-area ratio as shown in Figure 8. This relation is approximated by the regression curve, given as [13]

$$\langle b \rangle = 2.5 + 16.0 \exp(-(R_c - R_{c0})/20.0) \tag{26}$$

where $\langle b \rangle$ is the mean mechanical aperture, and R_c is the contact-area ratio. The initial aperture is set $18.5 \mu\text{m}$ because the hydraulic aperture evaluated from the companion flow-through experiment [13] started initially with this value.

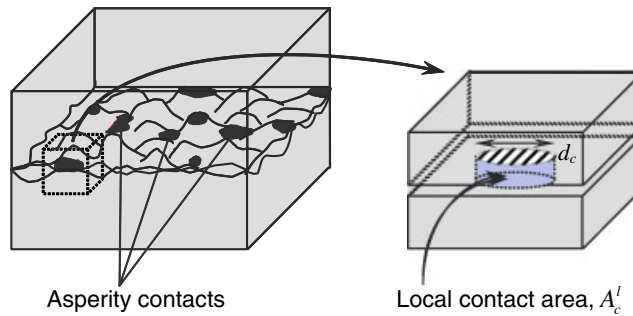


Figure 7. Idealized representation of asperity contact condition for lumped parameter model. A representative contact area A_c^l (right) represents the assumed average area of each contact (left), and is considered circular in shape of diameter d_c .

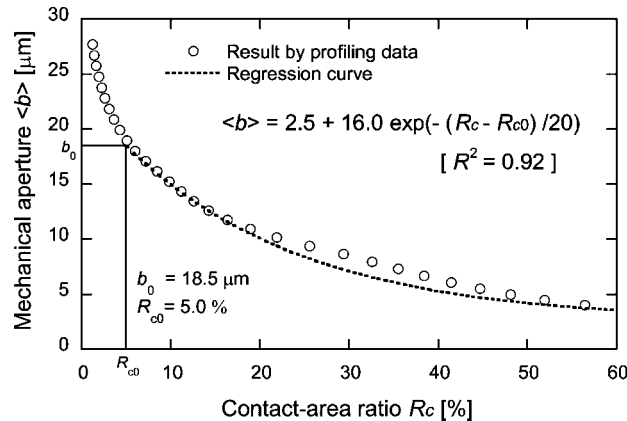


Figure 8. Relation between mean aperture and contact-area ratio. Circles are evaluated from point-by-point subtraction using the profiling data, and the dotted line is the regression curve of $\langle b \rangle = 2.5 + 16.0 \exp(-(R_c - R_{c0})/20)$ with the correlation coefficient, $R^2 = 0.92$.

A detailed description for the calculation procedure is reviewed in References [35, 37] and is also summarized in Appendix A. Parameters utilized in the predictions are listed in Table II. Predicted changes in fracture aperture and Si concentration are shown in Figure 9 together with the data measured through the experiments. Note that we omit the predictions during the reversed flow experiment (stage II) due to the unanticipated sharp reductions in aperture resulting from changes in fluid pressure distribution within the fracture by the switching of flow direction, which is not able to be predicted by the model. Thus, the unaccountable reduction is followed by resetting the aperture according to that recorded in the experiment and the contact-area ratio is updated using Equation (26). To closely match the evolution in fracture aperture in the experiment, the significant parameters of reaction rate constants $k_{+/-}$ for pressure dissolution (Equation (2)) and free-face dissolution (Equations (4) and (5)) are separately increased by factors shown in Table III. Also, the critical stress σ_c defined by Equation (3) is reduced by a factor of one-tenth to follow the large aperture reduction (~ 18.5 to ~ 10.0 μm) in the early experiment (0 to ~ 800 h); if the unmodified σ_c is used for the predictions, such a large decrease in aperture is not predicted because stress acting on contacts (i.e. σ_a) becomes equal to σ_c and then no further compaction proceeds (see Equation (2)). This indicates that critical stress σ_c may be smaller than that defined by Equation (3) and more data are needed to quantify this process. However, in this work we merely select a value of one-tenth σ_c in an attempt to replicate the experimental results.

As shown in Figure 9, the predictions of fracture aperture and Si concentrations using the augmented $k_{+/-}$ are in good agreement with the actual data although the applied multipliers are relatively large. Note that precipitation, which may reduce fracture aperture, exerts little influence on the change in aperture—solute concentration is much lower than equilibrium solubility as a result of the dominant effect of strongly advective transport and short residence time in the relatively short core (~ 10 cm). The multipliers applied to follow the experimental measurements are large, specifically for those in stages I–IV, implicating that other mechanisms may dominate over pressure solution and/or free-face dissolution, or the model may be incapable of representing the overall processes since a detailed topology for a fracture is not involved. This concern is further examined in the following section by accommodating a spatial distribution of contacts and apertures, using the FEM developed in this work.

3.2. Distributed parameter (numerical) model comparison

The numerical model developed in Section 2 is applied here to follow experimental observations of changes in fracture aperture and Si concentration. The latter are measured directly, and the former are inferred from measurements of flow rate and differential fluid pressure. The flow is along the long dimension of the image (Figure 1), from left to right, with no-flow boundaries applied along the two long sides, parallel to the flow direction of the fracture. Reasonable computational limits are placed on both memory and runtime—calculations are conducted using a constant element size of 2×2 mm². Note that even for this fine grid, local element Peclet numbers are of the order of 10^5 and result in a fully advection-dominant system.

Flow rates and parameters utilized in the predictions are summarized in Tables I and II. Predicted rates of aperture evolution and Si concentration history are matched with the actual measurements, as shown in Figure 10. Required modifications in parameters, necessary to replicate the experiments are listed in Table IV. Both the evolutions in fracture aperture and in Si concentration are in fairly good agreement with those observed. The predictions of Si

Table II. Parameters used to describe the evolution of fracture aperture.

Effective stress, σ_{eff} (MPa)	Diffusion path width, ω (nm)	Temperature, T ($^{\circ}\text{C}$)	Dissolution rate constant, k_{+} ($\text{mol m}^{-2} \text{s}^{-1}$)	Precipitation rate constant, k_{-} ($\text{mol m}^{-2} \text{s}^{-1}$)	Equilibrium solubility, C_{eq} (kg m^{-3})	Diffusion coefficient, D ($\text{m}^2 \text{s}^{-1}$)	Critical stress, σ_c (MPa)	Dynamic viscosity, μ (Pa s)
1.38	4.0	20	3.14×10^{-13}	2.46×10^{-9}	6.12×10^{-3}	2.04×10^{-10}	79.7	1.00×10^{-3}
		40	2.03×10^{-12}	8.85×10^{-9}	1.09×10^{-2}	2.91×10^{-10}	78.7	6.53×10^{-4}
		80	4.52×10^{-11}	7.43×10^{-8}	3.25×10^{-2}	5.24×10^{-10}	76.7	3.54×10^{-4}
		120	5.35×10^{-10}	4.04×10^{-7}	8.38×10^{-2}	8.36×10^{-10}	74.7	2.32×10^{-4}

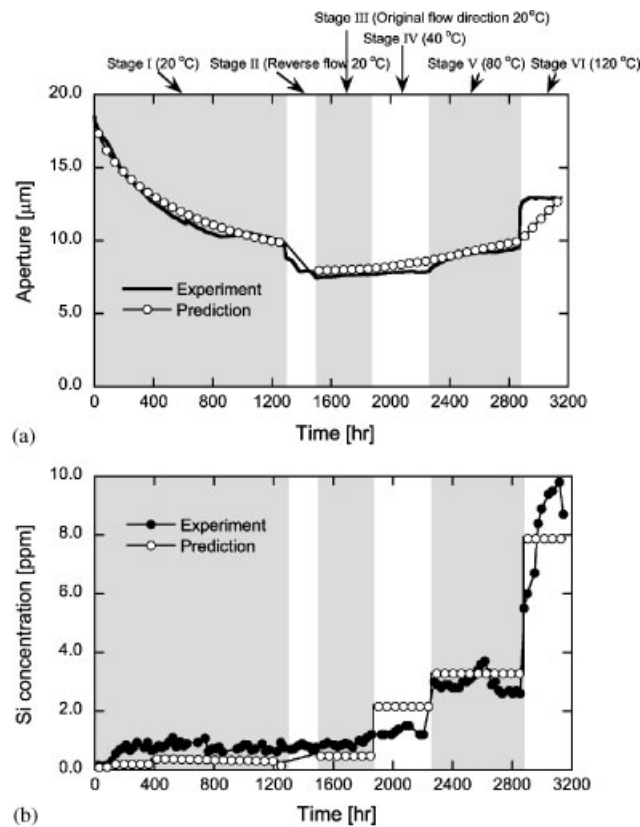


Figure 9. Comparisons of changes in: (a) aperture; and (b) Si concentration between the experimental results [13] and the predictions by the lumped parameter model. Open circles represent the predictions using modified values of reaction rate constants $k_{+/-}$ shown in Table III.

Table III. Experimental conditions and modification of parameters used in the analysis by the lumped parameter model.

Parameters	Test stages					
	I	II	III	IV	V	VI
Temperature (°C)	20	20	20	40	80	120
Flow direction	Original	Reversed	Original	Original	Original	Original
σ_c (Equations (2) and (3))	$\sigma_c \times 0.1$	$\sigma_c \times 0.1$	$\sigma_c \times 0.1$	$\sigma_c \times 0.1$	$\sigma_c \times 0.1$	$\sigma_c \times 0.1$
k_+ (Equation (2))	$k_+ \times 10^6$	—	$k_+ \times 10^4$	$k_+ \times 10^4$	$k_+ \times 500$	$k_+ \times 200$
$k_{+/-}$ (Equations (4) and (5))	$k_{+/-} \times 10^4$	—	$k_{+/-} \times 10^4$	$k_{+/-} \times 10^4$	$k_{+/-} \times 500$	$k_{+/-} \times 200$

concentrations, especially those during stages III and IV underestimate the real data; the predictions in stages III and IV are ~ 0.1 and ~ 0.2 ppm, relative to the measurements of ~ 0.9 and ~ 1.3 ppm, respectively. A systematic improvement in predictions between the lumped

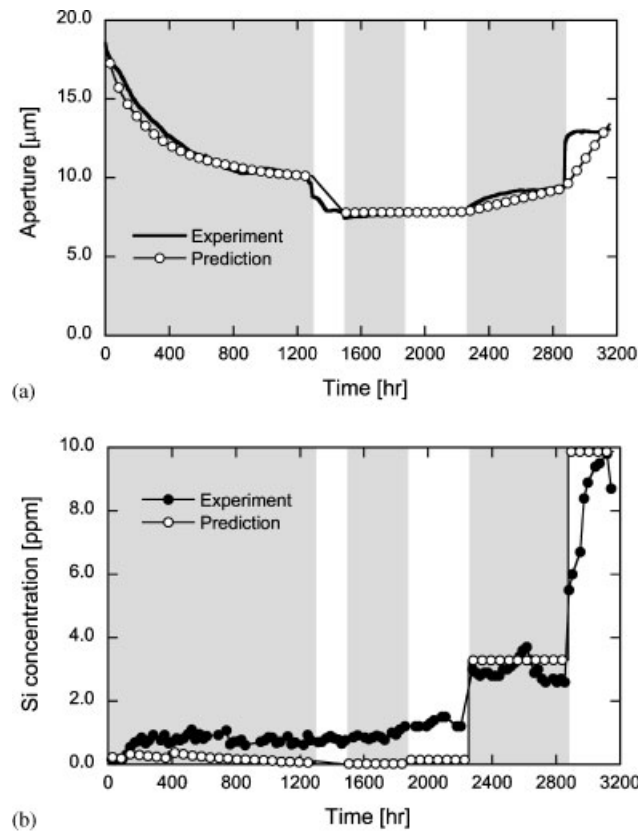


Figure 10. Comparisons of changes in: (a) aperture; and (b) Si concentration between the experimental results [13] and the predictions by the distributed parameter model developed in this work. Open circles represent the predictions using modified values of reaction rate constants $k_{+/-}$ shown in Table IV.

Table IV. Experimental conditions and modification of parameters used in the analysis by the distributed parameter (current) model.

Parameters	Test stages					
	I	II	III	IV	V	VI
Temperature (°)	20	20	20	40	80	120
Flow direction	Original	Reversed	Original	Original	Original	Original
σ_c (Equations (2) and (3))	$\sigma_c \times 0.1$	$\sigma_c \times 0.1$	$\sigma_c \times 0.1$	$\sigma_c \times 0.1$	$\sigma_c \times 0.1$	$\sigma_c \times 0.1$
k_+ (Equation (2))	$k_+ \times 5.0 \times 10^6$	—	$k_+ \times 30$	$k_+ \times 30$	$k_+ \times 30$	$k_+ \times 30$
$k_{+/-}$ (Equations (4) and (5))	$k_{+/-} \times 30$	—	$k_{+/-} \times 30$	$k_{+/-} \times 30$	$k_{+/-} \times 30$	$k_{+/-} \times 15$

parameter model and the numerical model is apparent in the applied multipliers for reaction rate constants to replicate the experiments (see Tables III and IV); the modifiers are much smaller for the numerical model—the small and constant magnitude multiplier of 30 is applied

throughout the experimental period except for pressure dissolution in stage I (i.e. 5.0×10^6) and for free-face dissolution/precipitation in stage VI (i.e. 15). However, the large multipliers required to replicate pressure dissolution during stage I (i.e. 10^6 for the lumped model and 5.0×10^6 for the numerical model) including the relatively abrupt and large aperture reduction, remain enigmatic. This implicates other mechanisms, such as mechanical creep and clogging resulting from locally high and unanticipated precipitation rates, of which neither are accommodated in the current description.

An important component of the model is the ability to follow the evolution in local aperture with time. Comparison between fracture apertures measured at the close of the experiment (3150 h) by X-ray CT [13], and those independently predicted by the model are shown in Figure 11. The white shaded area in the CT image represents apertures greater than the CT resolution threshold of $60 \mu\text{m}$. The scanning resolution for the X-ray CT is insufficient for a rigorous quantitative comparison between the CT image and the prediction. However, the model prediction is in qualitatively good agreement at several regions with large aperture (or void), with the CT image.

Flow patterns within the fracture are predicted with time and are shown at the beginning (0 h) and end (3150 h) of the experimental period (Figure 12). Flow velocities within the fracture at 0 h are entirely faster than those at 3150 h because of the larger flow rate prescribed (i.e. 1.0 vs $0.125 \text{ mL min}^{-1}$, see Table I). As apparent in Figure 12, flow at both times is tortuous due to the effects of surface roughness and contact area, and in particular the flow at the end is randomly

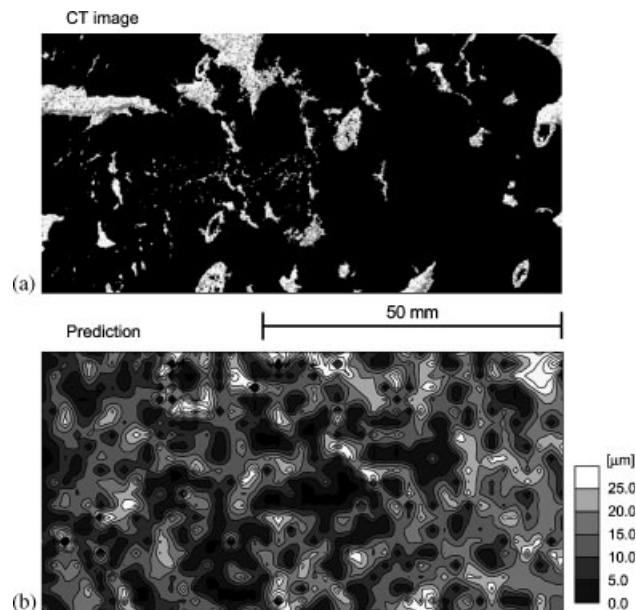


Figure 11. Qualitative comparison in aperture distribution between: (a) the X-ray CT image post-experiment (after Reference [13]); and (b) the predicted response at the end of simulation. (a) White coloured area represents aperture greater than the threshold of $60 \mu\text{m}$ and the black area shows aperture smaller than the threshold or contact area, while (b) white area is aperture greater than $25 \mu\text{m}$, with contact area shown in black.

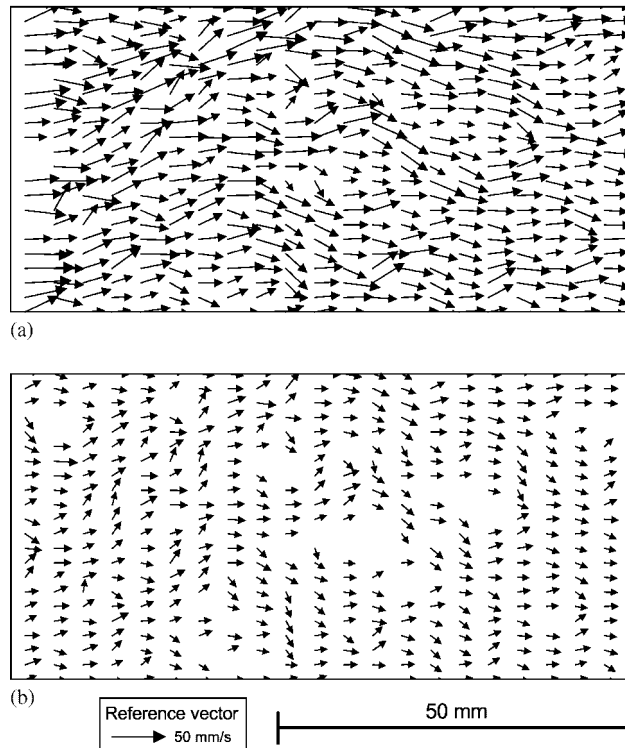


Figure 12. Flow field resulting from the FE solution of the Reynolds equation at: (a) 0 h; and (b) 3150 h. Vectors represent the relative magnitude and direction of local flow. Note that the flow is distributed randomly with flow-excluded zones growing with increased time, and related contact area.

distributed throughout the fracture without clear channelling although circumventing the regions of sufficiently small aperture and/or contact. Correspondingly, no preferential flow paths are generated during net-dissolution (or erosion) processes, which is congruent with the experimental measurements constrained by X-ray CT images and later Wood's metal injection [13]. This contrasts with other experiments where the evolution of flow channels formed through net dissolution [8, 12] are evident.

4. IMPLICATIONS OF EVOLUTION IN PERMEABILITY

Both the companion flow-through experiment [13] and the model predictions confirm that no preferential flow paths evolve within the fracture (i.e. pressure solution and free-face dissolution). This is likely due to the prescribed boundary conditions; the flow is injected throughout the fracture inlet with relatively high flow rates. In contrast, at the anticipated larger *in situ* scales of geothermal and petroleum reservoirs dissolution to enhance fracture permeability may not occur in the broad area throughout fractures of interest, but proceed

within the limited regions of fractures with preferential flow paths because flow is spatially restricted through limited numbers of injection and recovery wells.

To examine the effect of narrowed fluid injection relative to fracture length, which simply simulates fluid injection in geothermal and petroleum reservoirs, a simple numerical experiment is conducted. Injection into the same fracture is applied at a point ($Q = 1.0 \text{ mL min}^{-1}$ at the central node on the inlet boundary). The applied temperature is 120°C and the corresponding parameters for the prediction are listed in Table II. Predicted flow patterns within the fracture after 100 h, overlaying the distribution of fracture apertures are shown in Figure 13(a), together with the difference in apertures between 0 and 100 h, shown in Figure 13(b). Employing no modifications in reaction rate constants for this prediction, free-face dissolution dominates over the effect of pressure dissolution, resulting in the mean aperture consistently increasing at a rate of gaping of $3.7 \times 10^{-13} \text{ m s}^{-1}$ throughout the prediction. As apparent in Figure 13 several flow paths are generated during the 100 h virtual experiment, with net dissolution and erosion concentrated within the upper half of the plan-view of the fracture, generating a broad flow channel. This is likely due to the combined effect of the narrowed flow injection port and is sensitive to the initial conditions of the local aperture distribution (or roughness). Notably, the restricted flow presents a positive feedback that favours the development of localized flow conduits (worm-hole-like flow channels). Clearly, this effect is influenced by geometric factors relating to the scale of the sample—larger samples may develop multiple distributed flow channels with the ephemeral dominance of these channels switching with the progress of the transport network.

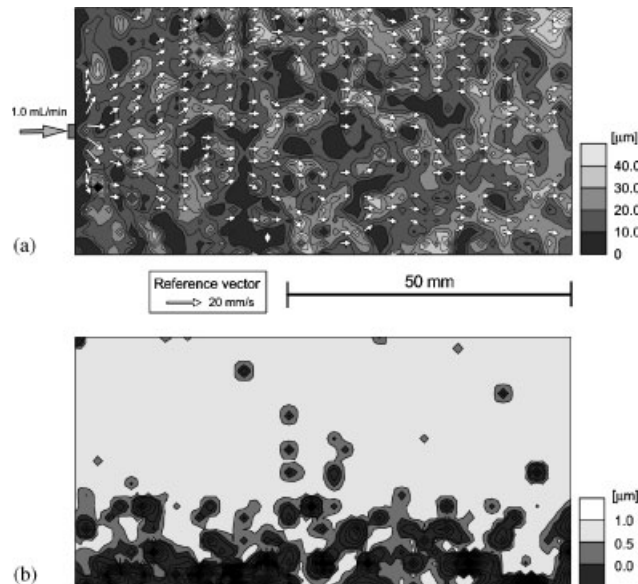


Figure 13. Results of numerical flow-through simulation at 100 h after flow started: (a) overlay of flow field on aperture contour. Note that several flow paths are formed; and (b) contour of aperture difference between 0 and 100 h. Lighter shading represent dissolution (erosion) regions.

5. CONCLUSIONS

A numerical model is developed to represent the evolution in fracture aperture mediated by the significant processes of pressure solution, and incorporating the serial processes of dissolution, diffusion, precipitation, and free-face dissolution. The model defines an initial distribution of fracture apertures, and supplements this with a Reynolds equation solution for the evolving flow-field—this flow-field is used to calculate the influence of chemical processes of pressure solution and free-face dissolution/precipitation in sequentially modifying the initial aperture distribution. Significantly, where advective flows dominate, as is anticipated to be the norm, the transport equation is solved via Lagrangian–Eulerian algorithm. The model is capable of predicting the evolution in aperture and solute concentration for a single fracture under arbitrary prescribed stress, temperature, and flow rate conditions. Predictions of both lumped parameter [35, 37] and distributed parameter representation of a single well-constrained experiment [13] are examined to test the adequacy of each model in representing experimentally observed behaviour. Notably, if the controlling parameters of reaction rate constants are increased by a factor of 30, the numerical model show excellent agreement with the experimental observations although a sharp reduction of the fracture aperture during the early experiment period is unable to be followed. This mismatch is likely attributed to processes of mechanical creep, that are not represented in the model. Both observations by X-ray CT, and model predictions, conclude that fluid flow at the conclusion of the experiment (3150 h) is broadly distributed throughout the fracture—no preferential flow paths are generated.

The model is applied to examine the evolution of fracture aperture (or permeability) where injection is concentrated at a point, as an approximation of injection into a reservoir. The predictions show the propensity to develop channelized dissolution features that concentrate flow. This exercise portends the potential to determine the form, plausible rates, magnitudes, and senses of permeability enhancement at field scale.

APPENDIX A: LUMPED PARAMETER MODEL

The evolution of fracture aperture is controlled by the competing influences of pressure solution, which incorporates interfacial dissolution, diffusion, and precipitation, and free-face dissolution. Interfacial dissolution at contacting asperities (Equation (2)) and free-face dissolution/precipitation (Equations (4) and (5)) are defined in the main text, and interfacial diffusion is defined herein in terms of the diffusive mass flux, dM_{diff}/dt , as [24]

$$\frac{dM_{\text{diff}}}{dt} = \frac{2\pi\omega D}{\ln(d_c/2a)}(C_{\text{int}} - C_{\text{pore}}) \quad (\text{A1})$$

where ω is the thickness of the water-film trapped at the interface, D is the diffusion coefficient, and $(C_{\text{int}})_{x=a}$ and $(C_{\text{pore}})_{x=d_c/2}$ are mineral concentrations in the interface fluid and pore space, respectively.

A single fracture is idealized as two rough surfaces held apart by bridging asperities, as illustrated in Figure 7 (left). The average contact-area ratio, R_c , may be determined by defining a representative contact area, A_c^1 , surrounded by an appropriate tributary area, A_t^1 , (Figure 7,

right), and is assumed equivalent to the ratio of the summed local contact areas, A_c^t , to the total fracture area, A_t^l , given as [35]

$$R_c = \frac{A_c^l}{A_t^l} = \frac{A_c^t}{A_t^t} \quad (\text{A2})$$

Within this tributary area, the contact diameter, d_c , of the local contact area, A_c^l , is defined as

$$d_c = \sqrt{\frac{4A_c^l}{\pi}} \quad (\text{A3})$$

For uniaxial compaction, the normal forces acting on the tributary area and the contacting asperity balance, yielding the stress applied at the contact area, σ_a , as

$$\sigma_{\text{eff}} \cdot A_t^l = \sigma_a \cdot A_c^l \Rightarrow \sigma_a = \frac{\sigma_{\text{eff}}}{R_c} \quad (\text{A4})$$

where σ_{eff} is the average macroscopic effective stress.

Interactive processes of pressure solution and free-face dissolution irreversibly alter the geometry of the fracture surfaces, and the relation between fracture aperture and contact area may be defined to follow this modification of the fracture aperture and contact-area ratio within the tributary domain. A simple, but physically viable, relation between them is defined as [35]

$$\langle b \rangle = a_1 + a_2 \exp(-(R_c - R_{c0})/a_3) \quad (\text{A5})$$

where $\langle b \rangle$ is the mean aperture, R_c is the contact-area ratio, and a_i ($i = 1, 2, 3$) is a constant. This curve is adopted as a straightforward and representative relation between fracture contact area and aperture, to define the phenomenology of fracture sealing/gaping by pressure solution/free-face dissolution.

A.1. Computational procedure

The individual processes of dissolution at asperity contacts, diffusion along interfacial water-film, and free-face dissolution/precipitation are combined to define the progress of aperture reduction of the fracture with time. In the initial condition, a small representative contact area is set with the initial aperture of the fracture. An effective stress is applied, as amplified by the tributary geometry, and during time step Δt , appropriate magnitudes of mass dissolution at the representative contact area, diffusion, and free-face dissolution/precipitation are simultaneously evaluated from Equations (2), (A1), (4), and (5), respectively. Physically, the dissolved mass evaluated from Equation (2) is supplied to the interface, and domain shortening (i.e. aperture reduction) proceeds as this mass passes along the interface by diffusion, as defined by Equation (A1). From the known magnitude of the diffusing mass, the updated contact area and aperture are calculated using the relation of Equation (A5) (the integration of Equation (A5) represents the volume that is removed, and its volume is matched by the diffused volume). A portion of the mass that diffuses to the pore fluid may deposit to the free surface of the fracture (Equation (5)), resulting in an additive reduction in fracture void volume. Alternately, net dissolution from the fracture wall (Equation (4)) and resulting enlargement of the void cavity will compete with the closure occasioned by the shortening of the bridging asperity. The dominant process will prescribe whether the fracture gapes or seals. This deposition or dissolution on the free surface is controlled by the relative concentration differential between the pore fluid solution and the equilibrium concentration of that fluid (Equations (4) and (5)). Concurrently, mineral

concentrations in the immobile fluid layer beneath the asperity contact, and the mobile fluid in the fracture void fluid are updated, as [35]

$$C_{\text{int}|_{t+\Delta t}} = \frac{(D_1 + V_p/2\Delta t) \cdot (dM_{\text{diss}}/dt + V_p/4\Delta t \cdot C_{\text{int}|_t}) + D_1 V_p/2\Delta t \cdot C_{\text{pore}|_t}}{(D_1 + V_p/4\Delta t) \cdot (D_1 + V_p/2\Delta t) - D_1^2} \quad (\text{A6})$$

where

$$D_1 = \frac{2\pi\varpi D_b}{\ln(d_c/2a)} \quad (\text{A7})$$

$$C_{\text{pore}} = \frac{1}{Q} \left(\frac{dM_{\text{diff}}}{dt} + \frac{dM_{\text{diss}}^{\text{FF}}}{dt} \right) \quad (\text{if } C_{\text{pore}} < C_{\text{eq}}) \quad (\text{A8})$$

$$C_{\text{pore}} = \frac{1}{Q} \left(\frac{dM_{\text{diff}}}{dt} - \frac{dM_{\text{prec}}}{dt} \right) \quad (\text{if } C_{\text{pore}} > C_{\text{eq}}) \quad (\text{A9})$$

and Q denotes the flow rate.

These relations are used iteratively to follow the evolution of dissolved concentrations in the fracture void, and resulting closure-history of the fracture.

NOMENCLATURE

A_c	area of local contact (m^2)
A_e	area of one element (m^2)
A_{pore}	area of fracture void (m^2)
b	local aperture (m)
$\langle b \rangle$	mean mechanical aperture (m)
C_{eq}	equilibrium solubility (kg m^{-3})
C_{out}	lumped concentration travelling out of domain (kg m^{-3})
C_{pore}	concentration in pore space (kg m^{-3})
D	diffusion coefficient ($\text{m}^2 \text{s}^{-1}$)
$E_{k_{+/-}}$	activation energy for dissolution/precipitation (J mol^{-1})
E_m	heat of fusion (J mol^{-1})
E_C	activation energy for solubility (J mol^{-1})
E_D	activation energy for diffusion (J mol^{-1})
$k_{+/-}$	dissolution/precipitation rate constant ($\text{mol m}^{-2} \text{s}^{-1}$)
M^p	forward-particle-tracked mass (kg)
M_{prec}	precipitation mass (kg)
$M_{\text{diss}}^{\text{FF}}$	dissolution mass at pore space (kg)
$M_{\text{diss}}^{\text{PS}}$	dissolution mass at contact area (kg)
M^*	Lagrangian mass (kg)
n	number of time steps (dimensionless)
n_c	number of contact nodes (dimensionless)
n_t	number of total nodes (dimensionless)
N_i	shape function at i th node (dimensionless)
p	fluid pressure (Pa)

Q	flow rate ($\text{m}^3 \text{s}^{-1}$)
R	gas constant ($\text{J mol}^{-1} \text{K}^{-1}$)
R_c	contact-area ratio (dimensionless)
T	temperature (K)
T_m	temperature of fusion (K)
V	fluid velocity (m s^{-1})
V_m	molar volume (m^3)
x	particle position (m)
x^*	fictitious particle position (m)

Greek letters

μ	fluid viscosity (Pa s)
ρ_g	density (kg m^{-3})
σ_a	contact stress (Pa)
σ_c	critical stress (Pa)
σ_{eff}	effective stress (Pa)

ACKNOWLEDGEMENTS

This work is a result of partial support under Grants DOE-DE-PS26-01NT41048, DOE-DE-FG36-04GO14289, and ARC DP0209425. This support is gratefully acknowledged.

REFERENCES

1. Morrow CA, Moore DE, Lockner DA. Permeability reduction in granite under hydrothermal conditions. *Journal of Geophysical Research* 2001; **106**:30 551–30 560.
2. Tenthorey E, Cox SF, Todd HF. Evolution of strength recovery and permeability during fluid–rock reaction in experimental fault zones. *Earth and Planetary Science Letters* 2003; **206**:161–172.
3. Moore DE, Lockner DA, Byerlee JD. Reduction of permeability in granite at elevated temperatures. *Science* 1994; **265**:1558–1561.
4. Beer NM, Hickman SH. Stress-induced, time-dependent fracture closure at hydrothermal conditions. *Journal of Geophysical Research* 2004; **109**:B02211, doi:10.1029/2002JB001782.
5. Lin W, Roberts J, Glassley W, Ruddle D. Fracture and matrix permeability at elevated temperatures. *Workshop on Significant Issues and Available Data. Near-field/Altered-zone coupled effects expert elicitation project*, San Francisco, November 1997.
6. Polak A, Elsworth D, Yasuhara H, Grader A, Halleck P. Permeability reduction of a natural fracture under net dissolution by hydrothermal fluids. *Geophysical Research Letters* 2003; **30**(20):2020, doi:10.1029/2003GL017575.
7. Durham WB, Bonner BP. Self-propping and fluid flow in slightly offset joints at high effective pressures. *Journal of Geophysical Research* 1994; **99**:9391–9399.
8. Durham WB, Bourcier WL, Burton EA. Direct observation of reactive flow in a single fracture. *Water Resources Research* 2001; **37**:1–12.
9. Dobson PF, Kneafsey TJ, Sonnenthal EL, Spycher N, Apps JA. Experimental and numerical simulation of dissolution and precipitation: implications for fracture sealing at Yucca Mountain, Nevada. *Journal of Contaminant Hydrology* 2003; **62–63**:459–476.
10. Bryant SL, Schechter RS, Lake LW. Interactions of precipitation/dissolution waves in ion exchange in flow through permeable media. *AIChE Journal* 1986; **32**:751–764.
11. Liu X, Ormond A, Bartko K, Li Y, Ortoleva P. A geochemical reaction-transport simulator for matrix acidizing analysis and design. *Journal of Petroleum Science and Engineering* 1997; **17**:181–196.
12. Polak A, Elsworth D, Liu J, Grader AS. Spontaneous switching of permeability changes in a limestone fracture with net dissolution. *Water Resources Research* 2004; **40**:W03502, doi:10.1029/2003WR002717.

13. Yasuhara H, Polak A, Mitani Y, Grader A, Haleck P, Elsworth D. Evolution of fracture permeability through fluid–rock reaction under hydrothermal conditions. *Earth and Planetary Science Letters* 2006, in press.
14. Neuman SP. Adaptive Eulerian–Lagrangian finite element method for advection–dispersion. *International Journal for Numerical Methods in Engineering* 1984; **20**:321–337.
15. Yeh GT. A Lagrangian–Eulerian method with zoomable hidden fine-mesh approach to solving advection–dispersion equations. *Water Resource Research* 1990; **26**(6):1133–1144.
16. Konikow LF, Goode DJ, Hornberger GZ. A three-dimensional method-of-characteristics-transport model (MOC3D). *Water-Resources Investigations Report 96-4267*, U.S. Geological Survey, Reston, VA, 1996.
17. Mitani Y, Esaki T, Zhou G, Nakashima Y. Experiments and simulation of shear-flow coupling properties of a rock joint. In *Proceedings of the 39th U.S. Rock Mechanics Symposium*, Culligan PJ, Einstein HH, Whittle AJ (eds). Cambridge, 2003; 1459–1464.
18. Piggott AR, Elsworth D. Laboratory assessment of the equivalent apertures of a rock fracture. *Geophysical Research Letters* 1993; **30**(13):1387–1390.
19. Pashley RM. Hydration forces between mica surfaces in electrolyte solutions. *Advances in Colloid and Interface Science* 1982; **16**:57–62.
20. Horn RG, Smith DT, Haller W. Surface forces and viscosity of water measured between silica sheets. *Chemical Physics Letters* 1989; **162**:404–408.
21. Brown SR. Fluid flow through rock joints: the effect of surface roughness. *Journal of Geophysical Research* 1987; **92**:1337–1347.
22. Zimmerman RW, Kumar S, Bodvarsson GS. Lubrication theory analysis of the permeability of rough-walled fractures. *International Journal of Rock Mechanics and Mining Sciences and Geomechanics Abstracts* 1991; **28**:325–331.
23. Brown SR, Stockman HW, Reeves SJ. Applicability of the Reynolds equation for modeling fluid flow between rough surfaces. *Geophysical Research Letters* 1995; **22**(18):2537–2540.
24. Yasuhara H, Elsworth D, Polak A. A mechanistic model for compaction of granular aggregates moderated by pressure solution. *Journal of Geophysical Research* 2003; **108**:B11, 2530, doi:10.1029/2003JB002536.
25. Heidug WK. Intergranular solid–fluid phase transformations under stress: the effect of surface forces. *Journal of Geophysical Research* 1995; **100**:5931–5940.
26. Revil A. Pervasive pressure-solution transfer: a poro-visco-plastic model. *Geophysical Research Letters* 1999; **26**:255–258.
27. Stephenson LP, Plumley WJ, Palciauskas VV. A model for sandstone compaction by grain interpenetration. *Journal of Sedimentary Petrology* 1992; **62**:11–22.
28. Steefel CI, Lasaga AC. A coupled model for transport of multiple chemical species and kinetic precipitation/dissolution reactions with application to reactive flow in single phase hydrothermal systems. *American Journal of Science* 1994; **294**(5):529–592.
29. Rimstidt JD, Barnes HL. The kinetics of silica–water reactions. *Geochimica et Cosmochimica Acta* 1980; **44**:1683–1699.
30. Dove PM, Crerar DA. Kinetics of quartz dissolution in electrolyte solutions using a hydrothermal mixed flow reactor. *Geochimica et Cosmochimica Acta* 1990; **54**:955–969.
31. Fournier RO, Potter RWII. An equation correlating the solubility of quartz in water from 25°C to 900°C at pressure up to 10,000 bars. *Geochimica et Cosmochimica Acta* 1982; **46**:1969–1973.
32. Rutter EH. The kinetics of rock deformation by pressure solution. *Philosophical Transactions of the Royal Society of London, Series A* 1976; **283**:203–219.
33. Tada R, Maliva R, Siever R. Rate laws for water-assisted compaction and stress-induced water–rock interaction in sandstones. *Geochimica et Cosmochimica Acta* 1987; **51**:2295–2301.
34. Revil A. Pervasive pressure solution transfer in a quartz sand. *Journal of Geophysical Research* 2001; **106**:8665–8686.
35. Yasuhara H, Elsworth D, Polak A. Evolution of permeability in a natural fracture: significant role of pressure solution. *Journal of Geophysical Research* 2004; **109**(B3):B03204, doi:10.1029/2003JB002663.
36. Lee VW, Mackwell SJ, Brantley SL. The effect of fluid chemistry on wetting textures in novaculite. *Journal of Geophysical Research* 1991; **96**:10 023–10 037.
37. Yasuhara H, Elsworth D, Polak A, Liu J, Grader A, Halleck P. Spontaneous permeability switching in fractures in carbonate: lumped parameter representation of mechanically- and chemically-mediated dissolution. *Transport in Porous Media* 2006, in press.